Available online at www.sciencedirect.com
SCIENCE DIRECT®
Journal of Solid State Chemistry 179 (2006) 551–562
JOURNAL OF SOLID STATE CHEMISTRY
www.elsevier.com/locate/jssc

A structure and phase analysis investigation of the "1:1" ordered A_2InNbO_6 perovskites ($A = Ca^{2+}$, Sr^{2+}, Ba^{2+})

V. Ting[a,*], Y. Liu[a], R.L. Withers[a], L. Norén[a], M. James[b], J.D. Fitz Gerald[c]

[a]*Research School of Chemistry, Australian National University, Canberra, ACT 0200, Australia*
[b]*Bragg Institute, Australian Nuclear Science and Technology Organisation, PMB 1 Menai, NSW 2234, Australia*
[c]*Research School of Earth Sciences, Australian National University, Canberra, ACT 0200, Australia*

Received 22 July 2005; received in revised form 4 November 2005; accepted 12 November 2005
Available online 22 December 2005

Abstract

The structures of the Ba_2InNbO_6, Sr_2InNbO_6 and Ca_2InNbO_6 "1:1" complex perovskites have been refined from neutron powder diffraction data. Both the $A = Ca$ and Sr compounds occur at room temperature in $P12_1/n1$ ($\mathbf{a} = \mathbf{a}_p + \mathbf{b}_p$, $\mathbf{b} = -\mathbf{a}_p + \mathbf{b}_p$, $\mathbf{c} = 2\mathbf{c}_p$) perovskite-related superstructures while the $A = Ba$ compound occurs in the $Fm\bar{3}m$, $a = 2a_p$, elpasolite structure type. In the case of the $A = Ca$ compound, an extensive $Ca_2[(Ca_{2x/3}In_{1-x}Nb_{x/3})Nb]O_6$ 'solid solution' field spanning compositions between $Ca_4Nb_2O_9$ and Ca_2InNbO_6 in the $CaO–InO_{3/2}–NbO_{5/2}$ ternary phase diagram is shown to exist. Under the conditions of synthesis used, the 'solid solution' field stops just short of the ideal 1:1 Ca_2InNbO_6 composition.

Keywords: Perovskite; Neutron analysis; Compositional solid solution

1. Introduction

The room temperature "1:1" $A_2In^{+III}Nb^{+V}O_6$ double perovskites ($A = Ba^{2+}$, Sr^{2+} and Ca^{2+}) have been the subject of recent interest due to their potential as visible-light driven photocatalysts [1] as well as for their microwave dielectric properties in the case of the $A = Ba$ and Sr compounds [2,3]. Despite this interest, their crystal structures have yet to be well determined.

Yin et al. [1] reported random ordering of the In^{3+} and Nb^{5+} ions on the perovskite *B*-sites of these compounds despite early structural investigations suggesting rock-salt type ordering [4,5]. A more recent electron diffraction investigation of these compounds [6] found that both the $A = Ca$ and Sr compounds occur in $P12_1/n1$ ($\mathbf{a} = \mathbf{a}_p + \mathbf{b}_p$, $\mathbf{b} = -\mathbf{a}_p + \mathbf{b}_p$, $\mathbf{c} = 2\mathbf{c}_p$, subscript p for perovskite parent sub-cell) perovskite-related superstructure phases (the most commonly observed room temperature structure for tilted, *B*-site ordered double perovskites [7,8]) while the $A = Ba$ compound occurs in the $Fm\bar{3}m$, $a = 2a_p$, elpasolite structure type (the most commonly observed room temperature structure for non-tilted, *B*-site ordered double perovskites [7,8]). Furthermore, bond valence sum calculations were used to explain why this should be so as well as to provide a useful first-order approximation to the structures of each of the compounds [6].

This paper began as a straightforward neutron diffraction structure refinement follow-up to the earlier electron diffraction and bond valence sum study [6]. For the $A = Ba$ and Sr compounds, this remained the case. For the $A = Ca$ compound, however, the neutron diffraction data revealed the presence of a small (but persistent) amount of In_2O_3 as a second phase in compounds with nominal composition Ca_2InNbO_6—suggesting that the ideal 2:1:1 compound could not be made as a pure single phase compound under our conditions of synthesis. This led to a detailed investigation of the $Ca_2InNbO_6–Ca_4Nb_2O_9$ (or $Ca_2[(Ca_{0.67}Nb_{0.33})Nb]O_6$) quasi-binary join and to the discovery of an extensive $(1–x)Ca_2[InNb]O_6 \cdot xCa_2[Ca_{2/3}Nb_{4/3}]O_6$ "solid solution" running virtually all the way from one end member to the other. Levin and colleagues [9,10] have recently reported the existence of extensive "solid solutions" along similar quasi-binary joins. Given the influence

*Corresponding author. Fax: +61 2 6125 0750.
E-mail address: vting@rsc.anu.edu.au (V. Ting).

0022-4596/$ - see front matter © 2005 Elsevier Inc. All rights reserved.
doi:10.1016/j.jssc.2005.11.012

of *B*-site cation ordering upon physical properties in complex perovskites [11], the results of a phase analysis and diffraction study of this "solid solution" are also presented in the current paper.

2. Experimental

Samples of nominal stoichiometry A_2InNbO_6, $A = Ba$, Sr and Ca, were synthesised using conventional solid-state synthesis. Stoichiometric amounts of $BaCO_3$ (4 N, Aldrich), $SrCO_3$ (5 N, Alfa) or $CaCO_3$ (5 N, Alfa) were mixed together with In_2O_3 (4 N, Aldrich) and Nb_2O_5 (4 N, Aldrich) and ground to a uniform powder under acetone in an agate mortar. The resultant mixtures were first thermally treated at 850 °C for a 20 h period, then pressed into pellets and calcined at 1230 °C for periods of 48 h with intermediate grinding and re-pelleting. In the $A = Ba$ and Sr cases, single-phase material of the desired stoichiometry resulted but not in the $A = Ca$ case (see below).

When it became clear that 'Ca_2InNbO_6' (composition 1 in Fig. 1) was unstable under the conditions of synthesis used and that the complex perovskite phase actually synthesised might represent one end member composition of a solid solution field, additional samples along the quasi-binary join between 'Ca_2InNbO_6' and $Ca_2[(Ca_{0.67}Nb_{0.33})Nb]O_6$ (see Fig. 1) were synthesised using $Ca(NO_3)_2 \cdot 4H_2O$ (98%, Univar) as a starting material in place of $CaCO_3$, also via solid state reaction.

Powdered samples of the sintered pastilles were checked for phase purity using X-ray powder diffraction (Guinier-Hägg XRD camera with a Cu$K\alpha_1$ radiation source). Silicon (NBS no. 640) was added as an internal standard for accurate determination of the unit cell dimensions which were refined using the Unitcell software package [12]. Transmission electron microscope (TEM) investigation was carried out on Philips EM 430 and CM30 TEM's on crushed grains of the samples dispersed onto holey carbon-coated copper grids.

Room temperature neutron powder diffraction data was collected on the A_2InNbO_6, $A = Ba$ and Sr, samples as well as on two of the samples (compositions 2 and 5 in Fig. 1) along the quasi-binary join from 'Ca_2InNbO_6' to $Ca_2[(Ca_{0.67}Nb_{0.33})Nb]O_6$. The data was collected over periods of 48–60 h using neutrons of wavelength 1.8835 Å over the 2θ range $10° < 2\theta < 135°$ employing a step size of 0.05° on the High Resolution Powder Diffractometer (HRPD) at the High Flux Australian Reactor (HIFAR) operated by the Australian Nuclear Science and Technology Organisation (ANSTO). The samples were run in 8 mm aluminium-capped vanadium annular cans to minimise the effect of neutron absorption by the indium in the samples. The data were refined using the Rietica Rietveld refinement package [13].

Elemental analyses were performed at 15 kV and 1 nA on a JEOL 6400 Scanning Electron Microscope (SEM) using Electron Probe Microanalysis (EPMA) in back-scattered geometry. Samples were prepared by mounting the powders in resin, polishing to a < 1 μm finish followed by the application of a thin carbon coat. NbO_2F, $InNbO_4$ and $CaMgSi_2O_6$ were used as calibration standards.

3. Results

3.1. The $(1-x)Ca_2[InNb]O_6 \cdot xCa_2[(Ca_{2/3}Nb_{1/3})Nb]O_6 \equiv Ca_2[(Ca_{2x/3}In_{1-x}Nb_{x/3})Nb]O_6$ system

3.1.1. Phase analysis

The discovery of the 'solid solution' in the $A = Ca$ case began with examination of a long-exposure XRD pattern of the nominally 'Ca_2InNbO_6' sample, which turned up weak reflections in addition to those of the majority, monoclinic, complex perovskite phase. These weak reflections (overlooked in the initial analysis of this material) were identified as belonging to an In_2O_3 second phase. Attempts to obtain a homogeneous Ca_2InNbO_6 powder by re-pelleting and annealing the sample for longer periods of time as well as at higher temperatures made no difference to the positions or intensities of the extra reflections. Likewise the use of different starting materials (CaO, $Ca(NO_3)_2 \cdot 4H_2O$) for the synthesis made little difference.

The fact that each of the nominal 'Ca_2InNbO_6' samples consistently contained a small, but reproducible, proportion of In_2O_3 implied that the majority perovskite phase (labelled composition 2 in Fig. 1) was the preferred product and that the ideal 'Ca_2InNbO_6' composition (composition 1 in Fig. 1) was unstable under the conditions of synthesis used. It was thus speculated that composition 2 might represent one end member composition of a solid solution field that could stretch all the way to $Ca_2[(Ca_{0.67}Nb_{0.33})Nb]O_6$ (composition 6 in Fig. 1). This prompted the synthesis and systematic structural investigation of three intermediate compositions along the quasi-binary join from 'Ca_2InNbO_6' to $Ca_2[(Ca_{0.67}Nb_{0.33})Nb]O_6$: $Ca_2[(Ca_{0.24}In_{0.64}Nb_{0.12})Nb]O_6$ (which will henceforth be referred to as composition 3), $Ca_2[(Ca_{0.40}In_{0.40}Nb_{0.20})Nb]O_6$ (composition 4) and a composition approaching $Ca_2[(Ca_{0.67}Nb_{0.33})Nb]O_6$, i.e. $Ca_2[(Ca_{0.50}In_{0.25}Nb_{0.25})Nb]O_6$ (labelled as compositions 3–5, respectively, in Fig. 1). Each of these compounds were synthesised using the more reactive $Ca(NO_3)_2 \cdot 4H_2O$ as a starting material, rather than $CaCO_3$.

From XRD, all three synthesised compositions appeared single phase with no trace of In_2O_3 visible on the Guinier films. This strongly supported the idea that it is possible to continuously change the composition of this complex perovskite phase from just short of Ca_2InNbO_6 all the way to $Ca_2[(Ca_{0.67}Nb_{0.33})Nb]O_6$.

3.1.2. Compositional analysis

EPMA analysis in the SEM was used to investigate the homogeneity and confirm the composition of all synthesised samples. In order to obtain a reasonable estimate of the reproducibility in these analyses, a significant number of spot analyses (usually 10) were performed and the

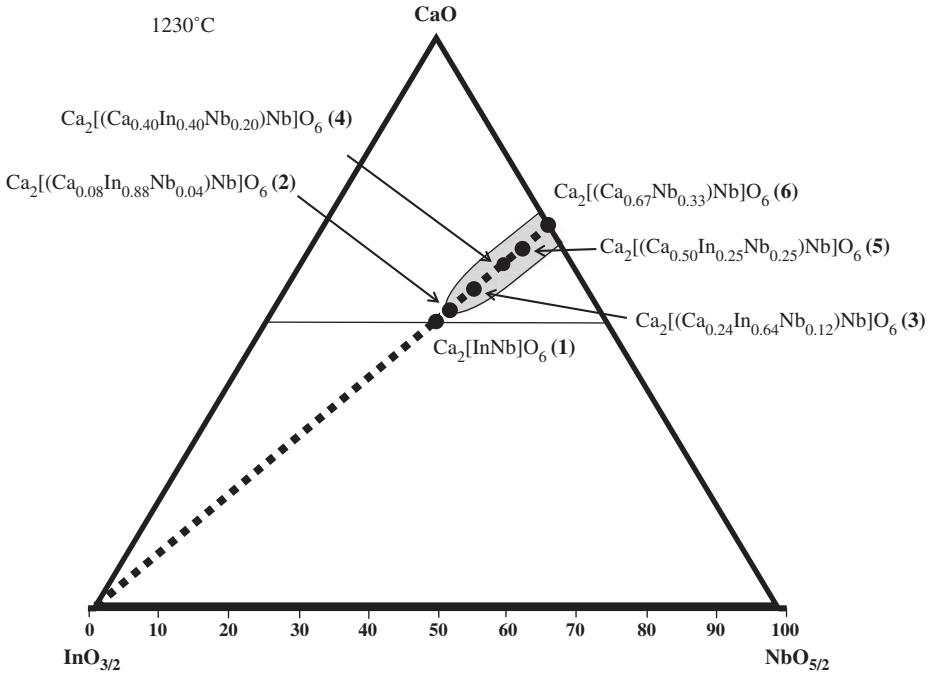

Fig. 1. Ternary phase diagram showing the compositions investigated, spanning the pseudo-binary join between Ca_2InNbO_6 and $Ca_2[(Ca_{0.67}Nb_{0.33})Nb]O_6$.

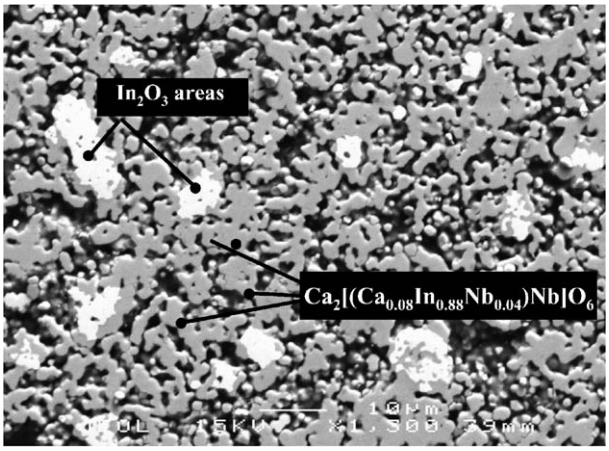

Fig. 2. A backscattered scanning electron microscopy image of the bulk Ca_2InNbO_6 material. The difference in contrast clearly shows the existence of two phases, the lighter areas corresponding to In_2O_3. The majority (indium-deficient) phase had an analysed composition of $Ca_{2.08(4)}In_{0.88(2)}Nb_{1.04(4)}O_6$ ($= Ca_2[(Ca_{0.08}In_{0.88}Nb_{0.04})Nb]O_6$).

averages were used. The standard deviations are quoted in brackets.

Back-scattered electron images of the nominally 'Ca_2InNbO_6' sample clearly showed the presence of the two distinct phases found by XRD for this material (see Fig. 2). The heavier (and more strongly scattering) In_2O_3 regions appear as lighter areas in the image while the darker areas correspond to the majority, In-deficient, complex perovskite phase. The composition of this majority phase turned out to be very close to 1:1, having an average stoichiometry over ten spot analyses of $Ca_{2.08(4)}In_{0.88(2)}Nb_{1.04(4)}O_6 = Ca_2[(Ca_{0.08}In_{0.88}Nb_{0.04})Nb]O_6$ (composition 2 in Fig. 1). Back-scattered electron imaging of the intermediate composition 3 and 4 samples confirmed them to be single phase with stoichiometries $Ca_{2.20(2)}In_{0.62(2)}Nb_{1.14(4)}O_6$ and $Ca_{2.38(2)}In_{0.39(1)}Nb_{1.22(2)}O_6$, respectively, in close agreement with the nominal stoichiometries. Likewise, back-scattered electron imaging of composition 5 (the composition approaching $Ca_3(CaNb_2)O_9$) also confirmed it to be a homogeneous material with a close to expected stoichiometry of $Ca_{2.43(3)}In_{0.26(1)}Nb_{1.27(2)}O_6$, or $Ca_3(Ca_{0.64(4)}In_{0.39(2)})Nb_{1.91(3)}O_9$.

These intermediate compounds follow the general substitution rule

$$3In^{3+} \leftrightharpoons 2Ca^{2+} + 1Nb^{5+},$$

whereby three In^{3+} ions can be substituted for a combination of two Ca^{2+} ions and one Nb^{5+} ion. The ideal stoichiometry of any member of the 'solid solution field' can thus be written in the form $Ca_2[(Ca_{2x/3}In_{1-x}Nb_{x/3})Nb]O_6$. Such a substitution mechanism appears to be operable not only because it preserves charge balance, but also because the combination of $\frac{2}{3}Ca^{2+}$ and $\frac{1}{3}Nb^{5+}$ has a similar average size to that of an In^{3+} ion [14].

3.1.3. Transmission electron microscopy

Single domain, selected area electron diffraction patterns (EDPs) typical of the end-member $Ca_2[(Ca_{0.08}In_{0.88}Nb_{0.04})Nb]O_6$ compound (composition 2 of Fig. 1) have already been reported (see Fig. 3 of [6]). They are consistent with a monoclinic $P12_1/n1$ ($\mathbf{a} = \mathbf{a}_p + \mathbf{b}_p$, $\mathbf{b} = -\mathbf{a}_p + \mathbf{b}_p$, $\mathbf{c} = 2\mathbf{c}_p$, subscript p for perovskite parent) unit cell. This is the most commonly observed room temperature structure for tilted, *B*-site ordered double perovskites (see

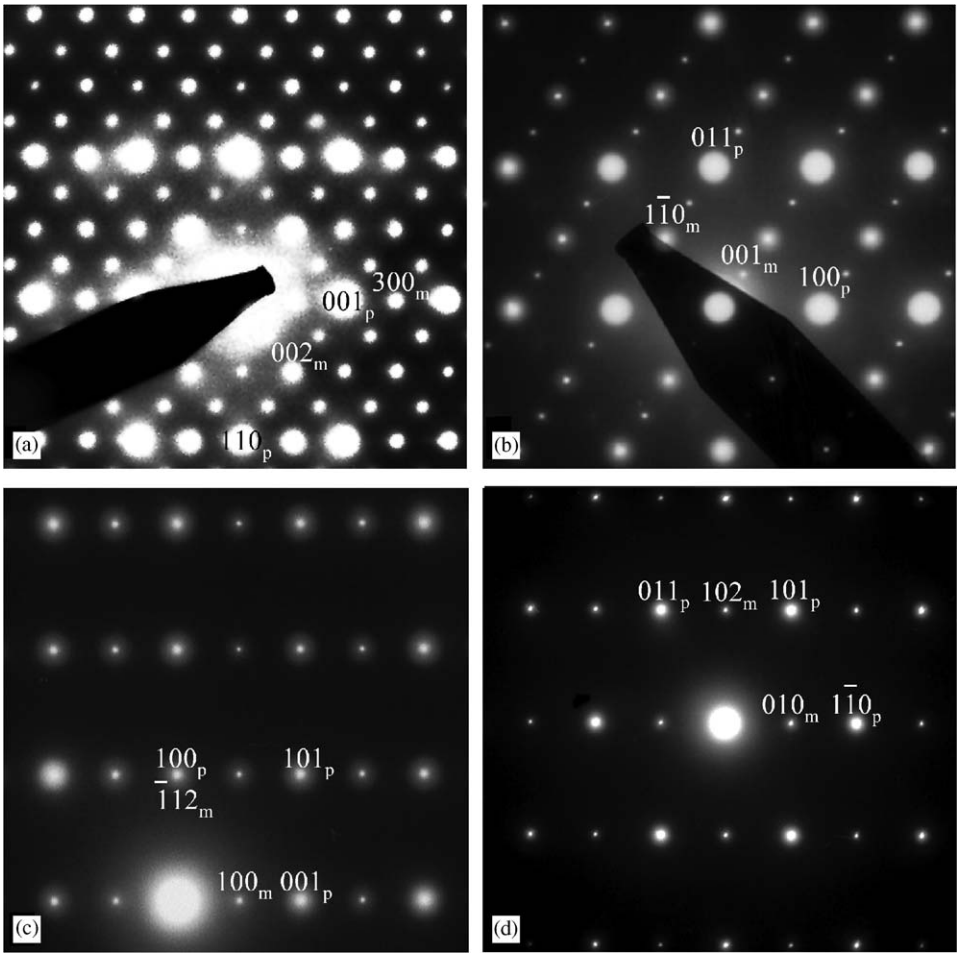

Fig. 3. (a) $[010]_m \equiv [1\bar{1}0]_p$, (b) $[110]_m \equiv [0\bar{2}2]_p$, (c) $[0\bar{2}1]_m \equiv [040]_p$ and (d) $[\bar{2}01]_m = [44\bar{4}]_p$ zone axis EDPs axes of composition 5 ($Ca_2[(Ca_{0.50}In_{0.25}Nb_{0.25})Nb]O_6$), indexed with respect with the underlying cubic perovskite parent cell (subscript p) as well as the true metrically monoclinic cell (subscript m), demonstrating that the structure of this material is isomorphous to that of Levin et al.'s $LT_{1/4}$ phase of $Ca_4Nb_2O_9$ (cf. with Fig. 7 of [16])).

e.g. [7,8]). Such a structure allows coupled octahedral rotation around both the **b**- and **c**-axis, i.e. a $(-b^-, b^-, c^+)$ tilt system in the notation originally developed by Glazer [15]) as well as octahedral *B*-site ordering and associated structural relaxation (see [6] for details).

Single domain, selected area EDPs typical of compositions at the other end of the 'solid solution' field such as $Ca_2[(Ca_{0.5}In_{0.25}Nb_{0.25})Nb]O_6$ (composition 5 in Fig. 1) are shown in Fig. 3. These EDPs are consistent with the $LT_{1/4}$, $\sqrt{6}a_p \times \sqrt{2}a_p \times 2\sqrt{2}a_p$ ($\mathbf{a}_m = -\mathbf{a}_p - \mathbf{b}_p + 2\mathbf{c}_p$, $\mathbf{b}_m = \mathbf{a}_p - \mathbf{b}_p$, $\mathbf{c}_m = 2\mathbf{a}_p + 2\mathbf{b}_p$; $\mathbf{a}_m^* = \frac{1}{2}[001]_p^*$, $\mathbf{b}_m^* = \frac{1}{2}[1\bar{1}0]_p^*$, $\mathbf{c}_m^* = \frac{1}{4}[111]_p^*$) superlattice recently reported by Levin et al. [16] as one of the polymorphs of $Ca_2[(Ca_{0.67}Nb_{0.33})Nb]O_6$ (i.e. $Ca_4Nb_2O_9$; cf. e.g. the EDPs given in Fig. 3 with those given in Fig. 7 of [16]). These EDPs strongly suggest that the two phases are structurally isomorphous. No extinction conditions are observed when indexed with respect to the above cell, requiring a primitive (*P*) cell and also ruling out the existence of glide planes perpendicular to the *b*-axis.

Despite the monoclinic metric symmetry, Levin et al. [16,17] have shown that the true space group symmetry of the $LT_{1/4}$ phase is triclinic *P*1 and described its crystal structure as ".. a combination of … octahedral tilting with $\mathbf{k} = \frac{1}{4}[111]_p^*$ ordering of Ca/Nb ordering on the *B*-sites..". This suggests that each of the structures across the $Ca_2[(Ca_{2x/3}In_{1-x}Nb_{x/3})Nb]O_6$ 'solid solution' field can be characterised by the same octahedral tilt system and differ only in the type and extent of the accompanying *B*-site ordering and associated structural relaxation (see below). Formally, however, the additional $\frac{1}{4}[111]_p^*$ modulation in the case of compositions closer to the $Ca_2[(Ca_{0.67}Nb_{0.33})Nb]O_6$ end-member composition means that we can no longer strictly speak of a continuous solid solution.

Fig. 4. (a) $[1\bar{1}0]_p$ zone axis EDPs of composition **2** {alt. written as $Ca_4[(Ca_{0.16}In_{1.76}Nb_{0.08})Nb_2]O_{12}$}, (b) from composition **3** {or $Ca_4[(Ca_{0.48}In_{1.28}Nb_{0.24})Nb_2]O_{12}$} and (c) from composition **4** {or $Ca_4[(Ca_{0.80}In_{0.80}Nb_{0.40})Nb_2]O_{12}$}, while (d) shows an $[01\bar{1}]_p$ zone axis EDP of composition **5** {or $Ca_4[(Ca_{1.0}In_{0.5}Nb_{0.5})Nb_2]O_{12}$}. All EDPs are indexed both with respect to the underlying parent perovskite sub-cell (subscript p) as well as the true unit cell (without any subscript), monoclinic $P2_1/n$ (in the cases of a–c, see above) and triclinic *P*1 (in the case of d). Note that the sharpness as well as the intensity of the

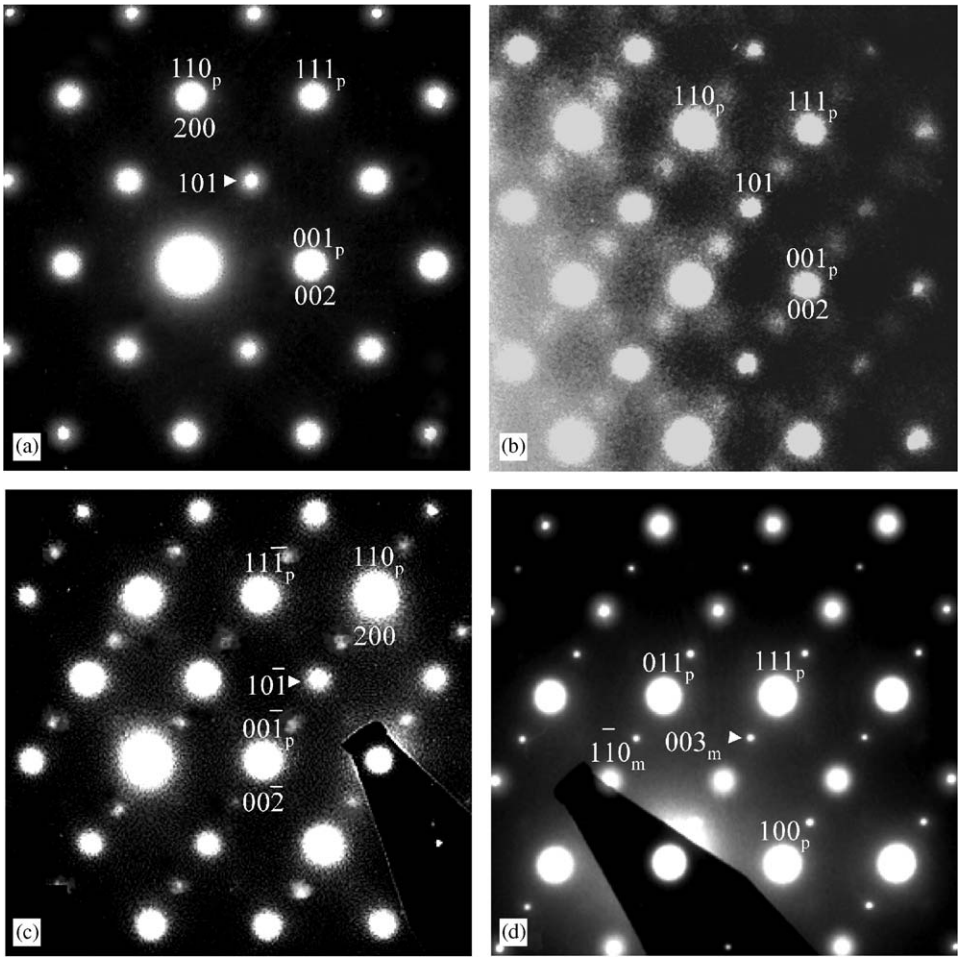

Fig. 4. [010]≡[$\bar{1}$10]$_p$ zone axis EDPs of (a) $Ca_2[(Ca_{0.08}In_{0.88}Nb_{0.04})Nb]O_6$, (b) $Ca_2[(Ca_{0.24}In_{0.64}Nb_{0.12})Nb]O_6$ and (c) $Ca_2[(Ca_{0.40}In_{0.40}Nb_{0.20})Nb]O_6$ along with the equivalent (d) [110]$_m$≡[0$\bar{2}$2]$_p$ zone axis EDP of $Ca_2[(Ca_{0.50}In_{0.25}Nb_{0.25})Nb]O_6$ indexed both with respect to the underlying cubic parent perovskite cell (subscript p) and the monoclinic $P2_1/n$ (in the case of a–c) and $P1$ (in the case of d) unit cells. As the composition changes from being closer to the 1:1 composition to closer to the 1:2 composition (in order a–d), note that the intensity as well as the sharpness of the $\mathbf{G}\pm1/4$ [111]$_p$* 'satellite reflections' systematically increases.

$\mathbf{G}\pm\frac{1}{4}$[111]$_p$* 'satellite reflections' increases as the composition moves from close to the ideal 1:1 Ca_2InNbO_6 composition closer to the ideal $Ca_2[(Ca_{0.67}Nb_{0.33})Nb]O_6$ end member composition (cf. e.g. Figs. 4a–d).

In the case of composition 2 (see Fig. 4a), there is no hint of intensity at the $\mathbf{G}\pm\frac{1}{4}\langle 111\rangle_p$* positions of reciprocal space. By composition 3 (see Fig. 4b), however, very weak diffuse blobs of intensity at these $\mathbf{G}\pm\frac{1}{4}\langle 111\rangle_p$* 'satellite reflection' positions become apparent. By composition 4 (which lies closer to the $Ca_2[(Ca_{0.67}Nb_{0.33})Nb]O_6$ end of the field), the $\mathbf{G}\pm\frac{1}{4}\langle 111\rangle_p$* 'reflections' are still very weak but noticeably sharper (c.f., e.g. Fig. 4c with b). At the $Ca_2[(Ca_{0.50}In_{0.25}Nb_{0.25})Nb]O_6$ or $Ca_4[(Ca_{1.0}In_{0.5}Nb_{0.5})Nb_2]O_{12}$ composition, the $\mathbf{G}\pm\frac{1}{4}$[111]$_p$* satellite reflections have become well-defined superstructure reflections. They can thus no longer be ignored and treated as diffuse scattering but rather must be treated as genuine Bragg reflections.

Following Levin et al. [16,17], the presence of these satellite reflections is attributed to additional *B*-site occupational ordering of Ca, In and Nb atoms on two out of the four [111]$_p$ *B*-containing planes (see Fig. 4b of [17]). Thus the ideal stoichiometry of the 'solid solution' is perhaps best written in the form $Ca_4[(Ca_{4x/3}In_{2-2x}Nb_{2x/3})Nb_2]O_{12}$, as is given in the immediately preceding paragraph for the various synthesised samples.

3.2. Neutron powder diffraction refinements

Neutron powder diffraction data were collected for the A_2InNbO_6, A = Ba and Sr, samples as well as for compositions 2 and 5 along the quasi-binary join from 'Ca_2InNbO_6' to $Ca_2[(Ca_{0.67}Nb_{0.33})Nb]O_6$ (see Fig. 1). The neutron powder profiles were refined in each case using the Rietica Rietveld refinement package [13]. Backgrounds were described using a Cheby II-type polynomial (six refineable parameters). Zero points and scale factors were refined. The starting unit cell parameters were taken from the XRD determined values. The wavelength used in the neutron refinements was $\lambda_{neutron} = 1.8835$ Å. The peak shape was described with a pseudo-Voigt peak profile using four free parameters.

Table 1
Refined atomic positions (x,y,z), isotropic thermals (B_{iso}) and fractional site occupancies (Occ) of the atoms in Ba_2InNbO_6 ($Fm\bar{3}m$, $a = 8.2819(2)$ Å)

Atom	x	y	z	B_{iso}	Occ	AV
Ba	0.2500	0.2500	0.2500	0.48(4)	1.00	2.14
	0.2500	0.2500	0.2500	0.74(4)	1.00	2.14
	0.2500	0.2500	0.2500	0.60(3)	1.00	2.03
In1	0.0000	0.0000	0.0000	0.31(4)	1.00	3.57
	0.0000	0.0000	0.0000	0.59(4)	0.75(3)	3.31
	0.0000	0.0000	0.0000	0.48(4)	0.76(4)	3.06
Nb1	0.5000	0.0000	0.0000	0.31(4)	1.00	4.15
	0.5000	0.0000	0.0000	0.59(4)	0.75(3)	4.49
	0.5000	0.0000	0.0000	0.48(4)	0.76(4)	4.86
O1	0.2528(4)	0.0000	0.0000	1.10(3)	1.00	2.00
	0.2563(3)	0.0000	0.0000	1.32(1)	1.00	2.01
	0.2598(5)	0.0000	0.0000	1.07(1)	0.76(6)	2.03
Nb2	—	—	—	—	—	—
	0.0000	0.0000	0.0000	0.59(4)	0.25(3)	3.39
	0.0000	0.0000	0.0000	0.48(4)	0.24(4)	4.86
In2	—	—	—	—	—	—
	0.5000	0.0000	0.0000	0.59(4)	0.25(3)	4.38
	0.5000	0.0000	0.0000	0.48(4)	0.24(4)	3.06
O2	—	—	—	—	—	—
	—	—	—	—	—	—
	0.7598(5)	0.0000	0.0000	1.07(1)	0.24(6)	2.03

The first row of values for each atom pertains to the results of the initial refinement, assuming In and Nb are fully rock-salt ordered. The second row shows the results of the anti-site refinement. The third row has the results of the stacking faulted anti-phase refinement.
1st row (simple refinement): $\chi^2 = 2.54$, $R_{Bragg} = 0.90$, $R_p = 4.58$, $R_{wp} = 5.87$.
2nd row (antisite refinement): $\chi^2 = 2.57$, $R_{Bragg} = 0.76$, $R_p = 4.59$, $R_{wp} = 5.91$.
3rd row (antiphase refinement): $\chi^2 = 2.44$, $R_{Bragg} = 0.95$, $R_p = 4.52$, $R_{wp} = 5.77$.

The occupancies were fixed so as to be consistent with the known compositions. The free atomic positional parameters and isotropic atomic displacement parameters (adp's) were then refined. The first three of the four neutron diffraction patterns showed additional peaks resulting from inadequate shielding of the aluminium in the sample can. The peaks belonging to this aluminium contamination phase were refined as a separate phase.

3.2.1. Ba_2InNbO_6

$Fm\bar{3}m$ space group symmetry allows rock-salt ordering of the In^{3+} and Nb^{5+} ions (at 000 and $00\frac{1}{2}$, respectively) on the perovskite B-sites of the doubled $a = 2a_p$ ($= 8.2819(2)$ Å) unit cell along with an associated shift of the O ions (at $00,\frac{1}{4}+\varepsilon_1$) away from the In^{3+} ions and towards the Nb^{5+} ions. For perfect In/Nb ordering, bond valence sum considerations suggest the value of this unknown oxygen fractional co-ordinate should be $(\frac{1}{4}+\varepsilon_1)\sim 0.2613$ (see [6]).

The experimental data was found to refine readily. The unknown oxygen fractional co-ordinate, however, refined to a value of 0.2528—noticeably lower than the value of 0.2613 predicted from bond valence sum considerations (see the first row of O1 fractional co-ordinate parameters in Table 1) and too low to be chemically plausible (the calculated apparent valence (AV) of the Nb ion, for example, is 4.15 instead of the expected 5.0 while that of the In ion is 3.57 instead of the expected 3.0—see the first row of parameters in Table 1). Additionally, although the observed intensities of the perovskite parent reflections matched well with the calculated intensities, the intensities of the satellite reflections $h\,k\,l$, h, k, l odd, were being systematically over calculated as the observed satellite peaks were significantly broader than calculated (see e.g. Fig. 5d).

These two observations were attributed to the presence of fine scale translational stacking faulting, i.e. to the presence of $\frac{1}{2}<100>\equiv<100>_p$ displacement faults. Such faulting effectively renormalises the extent of the In/Nb ordering as well as the shift of the O ions. Evidence for such faulting is apparent in both the broadening of the $h\,k\,l$, h, k, l odd, satellite reflections (see e.g. Fig. 5d) as well as in the existence of characteristic anti-phase boundary (apb)-type contrast on the scale of 20–50 nm apparent in $h\,k\,l$, h, k, l odd, superstructure dark field images (see Fig. 5a) but not in the equivalent bright field (see Fig. 5b) or parent perovskite dark field images. Faulting of a closely related sort has recently been shown to be characteristic of the $P\bar{3}m1$, but close to metrically cubic, $Ba_3CoNb_2O_9$ 1:2 ordered perovskite compound (see [18]).

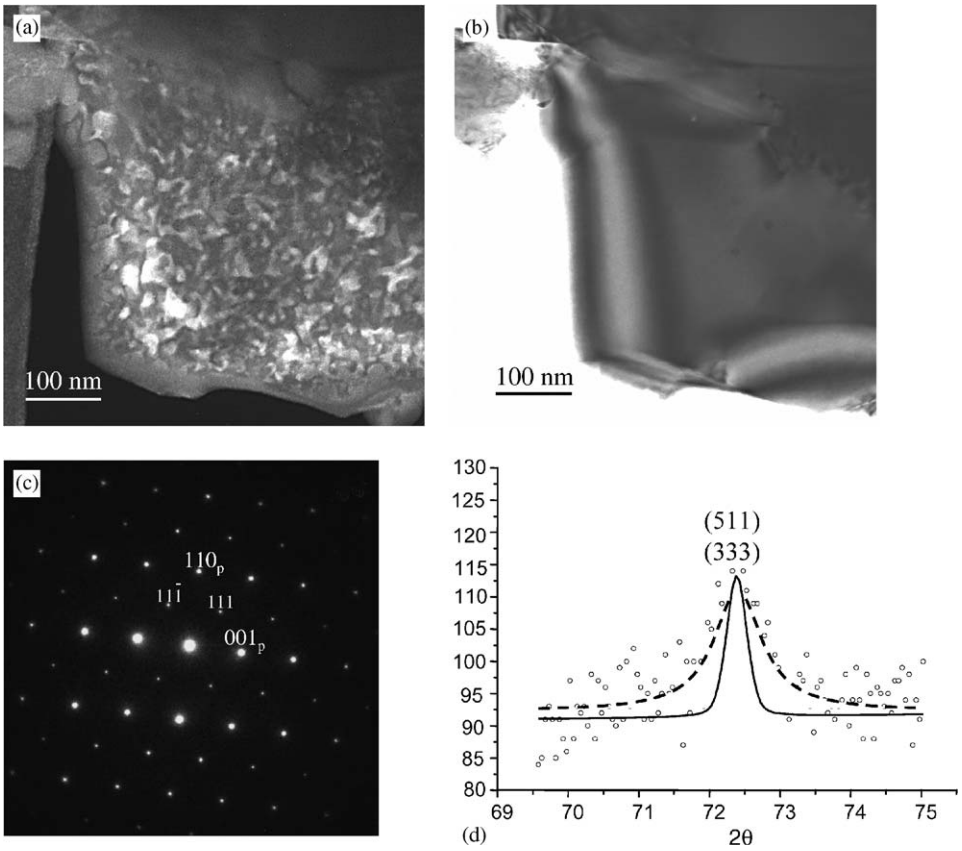

Fig. 5. (a) Typical superlattice dark field image taken near a $[110]_p$ zone axis orientation using the $[11\bar{1}]_p$ ($\equiv \mathbf{G} \pm \frac{1}{2}[111]_p^*$) type superstructure reflection (see (c)). Note the existence of characteristic anti-phase boundary (apb) domain contrast on the scale of 20–50 nm. (b) The same contrast is completely absent in parent perovskite dark field images or the corresponding bright field (BF) image shown in (b). The corresponding EDP is shown in (c). (d) An illustration of the broadening of the *h k l*, *h*, *k*, *l* odd, satellite reflections in Ba_2InNbO_6. The solid line is the peak shape obtained for the whole pattern refinement while the dashed line is a Lorentzian fit to the diffraction data for the [115]*/[333]* superstructure reflection. This broadening of the superlattice reflections is in agreement with the existence of fine-scale translational stacking faulting in this compound.

To test this, an anti-site refinement was performed by placing a proportion of In ions on the Nb *B*-site and vice versa and then refining the occupancies of the sites along with the unknown *x* fractional co-ordinate of the oxygen ion, O1 (see the second rows of Table 1). The fit to the satellite reflections thereby improved while the refinement statistics remained almost identical to those obtained for the initial refinement. The *x* coordinate for O1 refined to a value closer to that predicted from bond valence sum considerations (see [6]) while the occupancies refined to values which indicated that the proportion of *B*-site ions "exchanging" was roughly 25%. However, while an antisite refinement of this sort is easy to carry out and commonly reported for complex perovskites, such refinements are nonetheless entirely unrealistic as they imply that In^{3+} and Nb^{5+} ions can occupy the same local bonding environment. This crystal chemical nonsense can be seen clearly from the calculated AVs for this anti-site refinement given in the second row of Table 1. While the calculated AVs for In1 and Nb1 have become much more realistic (due to the increase in the *x*-coordinate of O1), those of their respective anti-site equivalents (In2 and Nb2) are clearly completely implausible.

A more realistic (stacking faulted) model can be obtained by adding a duplicate, coherently scattering, 'stacking faulted' structure translated by $\frac{1}{2}\langle 100\rangle \equiv \langle 100\rangle_p$ relative to the majority structure and then refining the relative occupancies of these two component structures. The fractional co-ordinates of all the atoms labelled with the number 2 in the third rows of Table 1 are thus obtained from those with the label 1 by the addition of $\frac{1}{2}$ to their *x* fractional co-ordinate. When this was done, the occupancies of the two component structures refined to values equivalent to a 3:1 ratio while the oxygen shift parameter refined to ~0.01 (see line 3 of Table 1 for the final refined atomic positions). As is shown in Table 1, the AVs of all atoms in the structure are now chemically plausible and in good agreement with the expected values. The refinement statistics at convergence were $\chi^2 = 2.44$, $R_{Bragg} = 0.95$, $R_p = 4.52$ and $R_{wp} = 5.77$ (Durbin Watson *d*-statistics 0.84/1.01). Fig. 6a shows the fit to the neutron powder profile.

Note that there was evidence for strain induced by orientational twinning and translational stacking faulting in that the peak shape varied with angle, becoming more asymmetric at higher values of 2θ (cf. e.g. Fig. 7a with b).

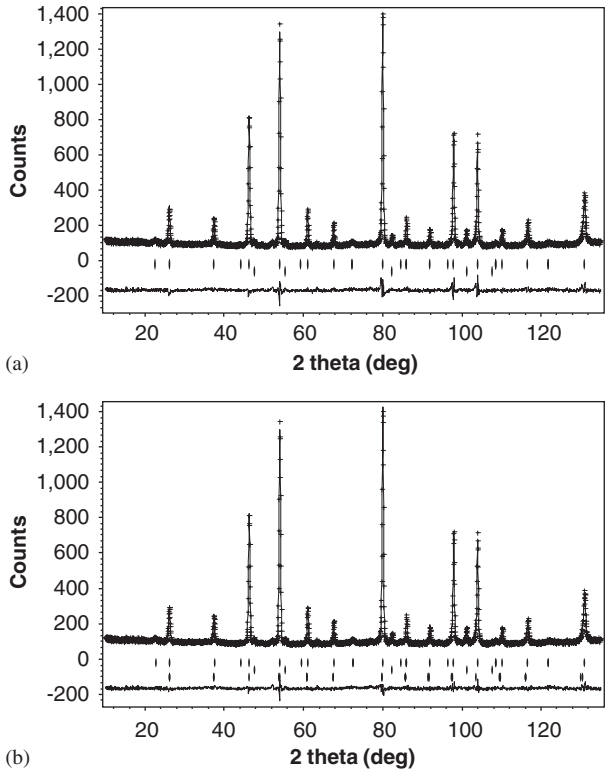

Fig. 6. The resultant neutron powder profile fits to Ba_2InNbO_6: (a) shows the stacking faulted model (the second set of peak markers in (a) and (b) are from the Al contamination phase). (b) Shows the stacking faulted refinement with an additional average perovskite tetragonal phase added to correct for the strain-induced peak asymmetry. Both plots show the data, fits as well as the difference profiles for the refinements.

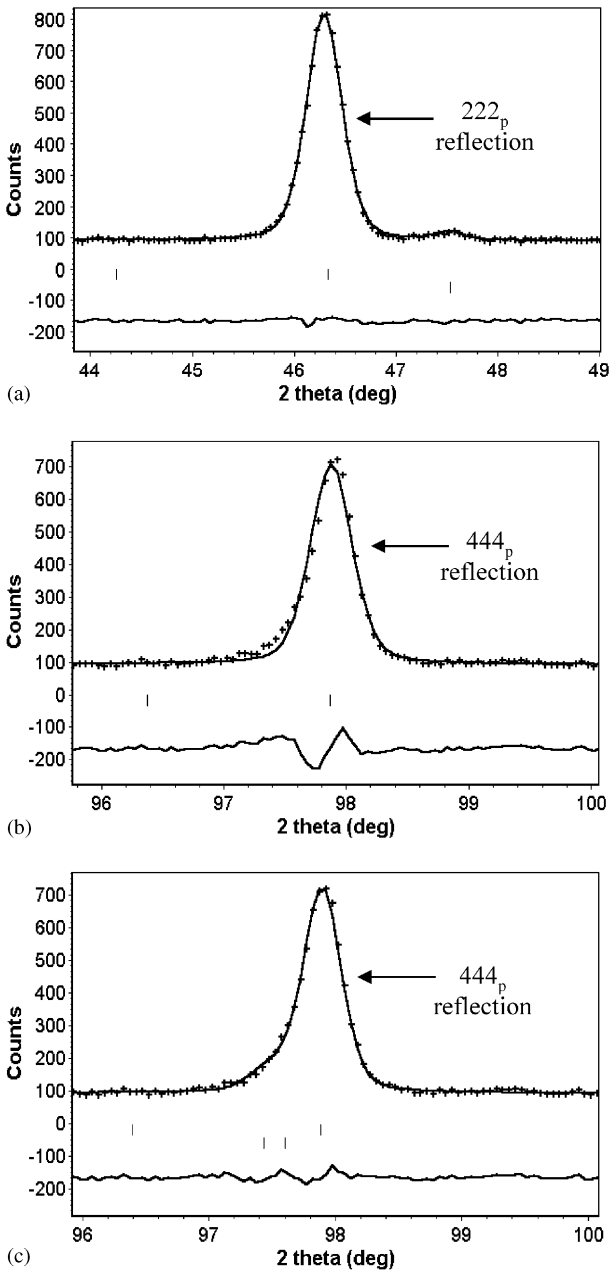

Fig. 7. Enlarged sections of the initial Ba_2InNbO_6 refinement profile showing (a) a low angle [222]* peak and (b) a high angle [444]* peak from the same profile. The pronounced asymmetry of the [444]* peak we believe results from microstructural strain. (c) Shows how the addition of a tetragonal, average perovskite 'phase' can correct for the asymmetry of the same high angle [444]* peak.

While Rietica allows for peak asymmetry, it does not allow for strain and size effects giving rise to 2θ-dependent peak asymmetry. In order to get a better fit to the data, it was clear that such effects would have to be modelled using an alternative approach.

A simple but effective way of doing this is to consider the effect stacking faulting might have on the perovskite parent unit cell in the vicinity of an apb, where the rock salt ordering of the larger InO_6-octahedra and the smaller NbO_6-octahedra must be locally broken. At the interface, a "bi-layer" must form where larger InO_6-octahedra and smaller NbO_6-octahedra are stacked on top of one another, introducing metric strain into the structure. To minimise this mismatch, InO_6 octahedra have to "compress" along an $<001>$ direction whilst NbO_6 octahedra would have to expand. Thus the simplest model is to allow for a small deviation of the parent unit cell symmetry from cubic to tetragonal. Thus a "second phase" based on a disordered perovskite parent (set in space group $P4/mmm$) was introduced in order to improve the fitting of the asymmetric parent reflections. This did indeed noticeably improve the fit to the high angle parent reflections (cf. e.g. the difference profile of Fig. 6b with that of a and Fig. 7c with b) as well as the refinement statistics when compared with the stacking faulted model given above to $\chi^2 = 1.79$, $R_{Bragg} = 0.88$, $R_p = 3.93$ and $R_{wp} = 4.93$ (Durbin Watson d-statistics 1.30/1.35). The addition of this second "phase", however, did not alter the refined co-ordinates obtained from the stacking faulted model. The refined profile is shown in Fig. 6b.

3.2.2. Sr_2InNbO_6

The monoclinic (but very close to metrically tetragonal) $P12_1/n1$ space group symmetry and $\mathbf{a} = \mathbf{a}_p + \mathbf{b}_p$,

$\mathbf{b} = -\mathbf{a}_p + \mathbf{b}_p$, $\mathbf{c} = 2\mathbf{c}_p$ unit cell of Sr_2InNbO_6 allows octahedral *B*-site ordering and associated coupled BO_6 octahedral expansion and contraction (described again by the parameter ε_1) as well as coupled BO_6 rigid body octahedral rotation around both the **b**- and **c**-axis (described by the parameters ε_2 and ε_3, respectively; see [6] for details). In terms of these three parameters, the predicted fractional co-ordinates of the three oxygens per asymmetric unit can be written as follows: O1 at $\frac{1}{4}+\varepsilon_1+\varepsilon_2$, $-\frac{1}{4}-\varepsilon_1+\varepsilon_2$, $0-\varepsilon_3$; O2 at ($\frac{1}{4}+\varepsilon_1-\varepsilon_2$, $\frac{1}{4}+\varepsilon_1+\varepsilon_2$, $0-\varepsilon_3$) and O3 at $0+2\varepsilon_3$, 0, $\frac{1}{4}+\varepsilon_1$, respectively (see [6]). Bond valence sum considerations (see [6]) predict $\varepsilon_1 \sim 0.0113$ and $\varepsilon_2 \sim \varepsilon_3 \sim 0.0352$. These predicted fractional co-ordinates (see the second line of fractional co-ordinates in Table 2) were used as starting fractional co-ordinates for the purposes of refinement.

In this refinement, in order to model the rigid body octahedral rotations, the movement of $O1_x$ was constrained to equal $O2_y$, i.e. $O1_x = O2_y$, $O2_x$ was constrained to equal $-O1_y$, i.e. $O2_x = -O1_y$ and $O3_x$ was constrained to equal -2 times $O1_z$ as well as -2 times $O2_z$, i.e. $O3_x = -2O1_z = -2O2_z$. $O3_y$ and $O3_z$ as well as the $Sr_{x,y,z}$ were allowed to refine independently. Note that this constrained refinement achieved refinement statistics (χ^2 and R_{Bragg} values) that were comparable to those obtained by unconstrained refinement of the oxygen positions, despite having nearly half the number of free parameters. Refinement with these constraints was straightforward and convergence rapid (see the first line of fractional co-ordinates in Table 2). The refinement statistics at convergence were $\chi^2 = 2.12$, $R_{Bragg} = 0.95$, $R_p = 4.52$ and $R_{wp} = 5.77$. Fig. 8 shows the fit to the neutron powder profile.

In terms of the ε parameters defined above, $\varepsilon_1 + \varepsilon_2$ refined to 0.0379, $-\varepsilon_1 + \varepsilon_2$ to 0.0257 (implying $\varepsilon_1 = 0.0061$ and $\varepsilon_2 = 0.0318$), ε_3 refined to 0.0337 while ε_1, as determined from $O3_z$, refined to 0.0106. The octahedral rotational amplitude parameters, $\varepsilon_2 = 0.0318$ and $\varepsilon_3 = 0.0337$, refine to ~93% of the bond valence sum predicted values $\varepsilon_2 \sim \varepsilon_3 \sim 0.0352$. The octahedral expansion and contraction parameter, ε_1, however, defined as the average between 0.0061 and $0.0106 = 0.0084$, refined to a somewhat smaller value of ~75% of the expected value of 0.0113. The calculated AVs of the In and Nb ions are thus ~0.3 valence units over-bonded and under-bonded relative to their ideal AVs (see Table 2). Given that the refined unit cell parameters ($a = 5.7351(2)$ Å, $b = 5.7416(2)$ Å, $c = 8.1102(3)$ Å, $\beta = 89.995(4)^\circ$) are very close to being metrically cubic ($a/\sqrt{2} = 4.0553$ Å, $b/\sqrt{2} = 4.0593$ Å, $c/2 = 4.0551$ Å with β very close to 90°), microstructural faulting might also be present in this $A = Sr$ compound. Note, however, that a simple translational stacking fault of, say, $\frac{1}{2}[001] \equiv [001]_p$ (as was appropriate in the case of the $A = Ba$ compound) would re-normalise the rotation around **b** parameter, i.e. ε_3, as well as the octahedral

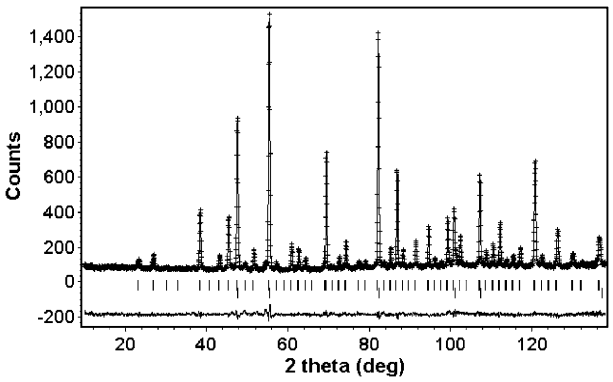

Fig. 8. The resultant neutron powder profile fits for Sr_2InNbO_6 (the second set of peak markers are again from the Al contamination phase). The plot shows the data, fits as well as the difference profiles for the refinement.

Table 2
Refined atomic positions (*x,y,z*), isotropic thermals (B_{iso}) and fractional site occupancies (Occ) of the atoms in Sr_2InNbO_6

Atom	*x*	*y*	*z*	B_{iso}	Occ	AV
Sr	0.5046(10)	−0.0214(3)	0.2486(11)	0.58(3)	1.00	1.96
	0.5000	0.0000	0.2500		1.00	
In	0.0000	0.0000	0.0000	0.34(2)	1.00	3.29
	0.0000	0.0000	0.0000		1.00	
Nb	0.5000	0.5000	0.0000	0.34(2)	1.00	4.68
	0.5000	0.5000	0.0000		1.00	
O1	0.2879(10)	0.7757(11)	0.9663(10)	0.83(2)	1.00	1.97
	0.2965	0.7739	0.9648		1.00	
O2	0.2243(11)	0.2879(10)	0.9663(10)	0.83(2)	1.00	1.96
	0.2261	0.2964	0.9648		1.00	
O3	0.0674(10)	0.0134(8)	0.2606(12)	0.83(2)	1.00	2.00
	0.0704	0.0000	0.2613		1.00	

Space group $P12_1/n1$, $a = 5.7351(2)$ Å, $b = 5.7416(2)$ Å, $c = 8.1102(3)$ Å, $\beta = 89.995(4)^\circ$. The first row of values for each atom pertains to the results of the refinement, assuming In and Nb are fully rock-salt ordered. The second row shows the starting values for the refinement, taken from [6].
Refinement statistics: $\chi^2 = 2.12$, $R_{Bragg} = 0.95$, $R_p = 4.52$, $R_{wp} = 5.77$.

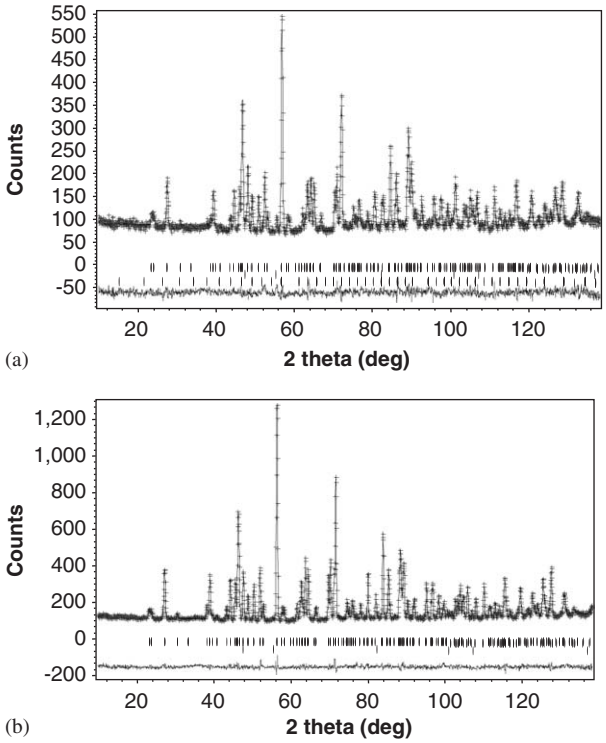

Fig. 9. The resultant neutron powder profile fits for (a) $Ca_2[(Ca_{0.08}In_{0.88}Nb_{0.04})Nb]O_6$ (the second set of peak markers are again from the Al contamination phase while the third set are from the In_2O_3 impurity phase) and (b) $Ca_2[(Ca_{0.50}In_{0.25}Nb_{0.25})Nb]O_6$ (the second set of peak markers are again from the Al contamination phase). Both plots show the data, fits as well as the difference profiles for the refinements.

expansion/contraction parameter ε_1 while leaving the octahedral rotation around **c** parameter, ε_2, unchanged (see e.g. Fig. 9 of [6]) and hence is not what is required. Likewise, a simple translational stacking fault of, say, $\frac{1}{2}[101] \equiv [010]_p$ would re-normalise all three ε parameters and again not what is required.

An additional anti-site refinement (of the sort performed on the Ba_2InNbO_6 compound) was carried out on the $A = Sr$ compound to give some indication as to the likelihood of microstructural faulting. Refinement of the coupled site occupancies of the *B*-site cations indicated that approximately 10% of the In/Nb cations were "exchanging" sites. As just discussed above, however, the addition of coupled octahedral rotations in the case of Sr_2InNbO_6 makes it difficult to envisage an appropriate microstructurally faulted model.

3.2.3. $Ca_2[(Ca_{0.08}In_{0.88}Nb_{0.04})Nb]O_6$

The space group symmetry and unit cell of this Ca compound are identical to those of the $A = Sr$ compound and hence most of the first paragraph of Section 3.2.2 above also applies in this case. The only difference is that the bond valence sum predicted values for $\varepsilon_1 \sim 0.0113$ and $\varepsilon_2 \sim \varepsilon_3 \sim 0.0530$ are larger than for the $A = Sr$ compound. Bear in mind, however, that these predicted fractional co-ordinates assumed ideal Ca_2InNbO_6 stoichiometry instead of the actual $Ca_2[(Ca_{0.08}In_{0.88}Nb_{0.04})Nb]O_6$ stoichiometry.

These predicted fractional co-ordinates (see the second line of fractional co-ordinates in Table 3) were used as starting fractional co-ordinates for the purposes of refinement. Refinement was carried out following the same procedure as described in the case of the $A = Sr$ compound except for the necessary inclusion of In_2O_3 as a second phase.

At the 1:1 stoichiometry, systematic discrepancies between the predicted and observed intensities of the parent perovskite peaks in the diffraction pattern were identified. As the intensities of these parent perovskite reflections (particularly at low angle) are almost exclusively determined by the stoichiometry of the sample, it was clear that the occupancies of the atomic sites needed to be refined. This resulted in the occupancy of the In on the 4*a* site at 0,0,0 refining to a value greater than unity. As the neutron scattering length for Nb (7.054 fm [5]), is far higher than that of either the Ca (4.70 fm) or the In (4.065 fm), this indicates that there is a proportion of Nb sharing the site. The values for the occupancies were then set at the values obtained from the EPMA determined stoichiometry of $Ca_2[(Ca_{0.08}In_{0.88}Nb_{0.04})Nb]O_6$. The pattern was found to refine very well with these values. The final refinement statistics at convergence for this $Ca_2[(Ca_{0.08}In_{0.88}Nb_{0.04})Nb]O_6$ compound were $\chi^2 = 2.01$, $R_{Bragg} = 1.47$, $R_p = 4.44$ and $R_{wp} = 5.61$ (for a refined cell with $a = 5.5292(2)$ Å, $b = 5.7068(2)$ Å, $c = 7.9216(3)$ Å, $\beta = 89.9243(4)^\circ$). The final refined fractional co-ordinates are given in the first lines of Table 3 while the profile fit is shown in Fig. 9a (the Al contamination phase corresponds to the second set of peak markers in Fig. 9a while the In_2O_3 second phase corresponds to the third set of peak markers). The In_2O_3 phase refined to 5.7(4)% of the total by weight and 0.9(7) mole%.

In terms of the ε parameters defined above, $\varepsilon_1 + \varepsilon_2$ refined to 0.0582, $-\varepsilon_1 + \varepsilon_2$ to 0.0430 (implying $\varepsilon_1 = 0.0076$ and $\varepsilon_2 = 0.0506$), ε_3 refined to 0.0520 while ε_1, as determined from $O3_z$, refined to 0.0062. The refined octahedral rotational amplitude parameters, $\varepsilon_2 = 0.0506$ and $\varepsilon_3 = 0.0520$, are again in very good accord with the bond valence sum predicted values $\varepsilon_2 \sim \varepsilon_3 \sim 0.0530$ while the refined octahedral expansion and contraction parameter, ε_1, defined as the average between 0.0076 and $0.0062 = 0.0069$, again refined to a value somewhat smaller than the expected value of 0.0113.

3.2.4. $Ca_4[(Ca_{1.0}In_{0.5}Nb_{0.5})Nb_2]O_{12}$

The neutron scattering data for $Ca_4[(Ca_{1.0}In_{0.5}Nb_{0.5})Nb_2]O_{12}$, despite the presence of clear $\mathbf{G}_p \pm \frac{1}{4}[111]_p^*$ satellite reflections in EDPs (see e.g. Fig. 3d), could nonetheless still be well fitted by the same monoclinic $P12_1/n1$ space group and $\mathbf{a} = \mathbf{a}_p + \mathbf{b}_p$, $\mathbf{b} = -\mathbf{a}_p + \mathbf{b}_p$, $\mathbf{c} = 2\mathbf{c}_p$ unit cell used for the $Ca_2[(Ca_{0.08}In_{0.88}Nb_{0.04})Nb]O_6$ compound. In particular, all the peaks in the profile were thereby accounted for (see Fig. 9b). As the $\mathbf{G}_p \pm \frac{1}{4}[111]_p^*$ satellite reflections

Table 3
Refined atomic positions (x,y,z), isotropic thermals (B_{iso}) and site occupancies (Occ) of the atoms in $Ca_2[(Ca_{0.08}In_{0.88}Nb_{0.04})Nb]O_6$

Atom	x	y	z	B_{iso}	Occ
Ca	0.5093(9)	−0.0486(5)	0.2524(10)	1.11(8)	1.00
	0.5000	0.0000	0.2500		1.00
In	0.0000	0.0000	0.0000	0.39(7)	0.88
	0.0000	0.0000	0.0000		1.00
Nb	0.0000	0.0000	0.5000	0.39(7)	0.50
	0.0000	0.0000	0.5000		0.50
O1	0.3082(11)	0.7930(12)	0.9480(19)	0.69(5)	1.00
	0.3133	0.7907	0.9480		1.00
O2	0.2070(12)	0.3082(12)	0.9480(17)	0.69(5)	1.00
	0.2093	0.3133	0.9480		1.00
O3	0.1040(6)	0.0366(13)	0.2562(10)	0.69(5)	1.00
	0.1040	0.0000	0.2613		1.00
Nb2	0.0000	0.0000	0.0000	0.39(7)	0.04
	—	—	—	—	—
Ca2	0.0000	0.0000	0.0000	0.39(7)	0.08
	—	—	—	—	—

Space group $P12_1/n1$, $a = 5.5292(2)$ Å, $b = 5.7068(2)$ Å, $c = 7.9216(3)$ Å, $\beta = 89.9243(4)^\circ$. The second row shows the starting values for the refinement, taken from [6].
Refinement statistics: $\chi^2 = 2.01$, $R_{Bragg} = 1.47$, $R_p = 4.44$, $R_{wp} = 5.61$.

observed in the TEM were not visible in the neutron powder profile, it was deemed unreasonable to lower the space group symmetry and unit cell from monoclinic $P12_1/n1$, $\mathbf{a} = \mathbf{a}_p + \mathbf{b}_p$, $\mathbf{b} = -\mathbf{a}_p + \mathbf{b}_p$, $\mathbf{c} = 2\mathbf{c}_p$ to the true $P1$, $\mathbf{a} = -\mathbf{a}_p - \mathbf{b}_p + 2\mathbf{c}_p$, $\mathbf{b} = \mathbf{a}_p - \mathbf{b}_p$, $\mathbf{c} = 2\mathbf{a}_p + 2\mathbf{b}_p$ cell. It should be noted, however, that this is an average structure refinement only of this material.

The occupancies of the various sites in the refined $P12_1/n1$ structure were set at the known stoichiometry, i.e., $Ca_2[(Ca_{0.50}In_{0.25}Nb_{0.25})Nb]O_6$ and the refinement again remained stable. The final refinement statistics at convergence were $\chi^2 = 2.26$, $R_{Bragg} = 2.01$, $R_p = 3.82$ and $R_{wp} = 4.78$ for a refined cell with $a = 5.5477(2)$ Å, $b = 5.7470(2)$ Å, $c = 7.9714(3)$ Å, $\beta = 89.958(3)^\circ$). The final refined fractional co-ordinates are given in the first lines of Table 4 while the final profile fit is shown in Fig. 9b.

In terms of the ε parameters defined above, $\varepsilon_1 + \varepsilon_2$ refined to 0.0650, $-\varepsilon_1 + \varepsilon_2$ to 0.0396 (implying $\varepsilon_1 = 0.0127$ and $\varepsilon_2 = 0.0523$), ε_3 refined to 0.0531 while ε_1, as determined from $O3_z$, refined to 0.0097. The refined octahedral rotational amplitude parameters, $\varepsilon_2 = 0.0523$ and $\varepsilon_3 = 0.0531$, are very similar to those refined for $Ca_2[(Ca_{0.08}In_{0.88}Nb_{0.04})Nb]O_6$ and show that not only does the same $(-b^-, b^-, c^+)$ rotation scheme apply but the refined amplitudes of the octahedral rotations around the resultant **b**- and **c**-axis remain virtually the same across the 'solid solution'. Deconvoluting these octahedral rotation angles from the refined positional parameters shows that the angles of rotation are ~11.0° around **c** and (~$\sqrt{2} \times 11.0^\circ$) ~15.9° around **b** for $Ca_2[(Ca_{0.08}In_{0.88}Nb_{0.04})Nb]O_6$ and ~11.3° around **c** and (~$\sqrt{2} \times 11.3^\circ$) ~16.2° around **b** for $Ca_{1.96}[(Ca_{0.46}In_{0.26}Nb_{0.28})Nb]O_6$. These refined rotation angles are also similar to those predicted for the ideal 1:1 Ca_2InNbO_6 structure (of ~11.7° around **c** and ~16.5° around **b**) and also those refined for the $LT_{1/4}$ $Ca_4Nb_2O_9$ (i.e. $Ca_2[(Ca_{0.67}Nb_{0.33})Nb]O_6$) end member [16,17]. The only real difference in moving across the 'solid solution' field appears to be the additional B-site ordering associated with In and Nb versus Ca ordering onto every second $[111]_p$ plane giving rise to the $\mathbf{G}_p \pm 1/4$ $[111]_p^*$ satellite reflections apparent in EDPs of samples with high Ca content (see e.g. Fig. 3d).

4. Conclusions

The crystal structures of the 1:1 complex perovskites Ba_2InNbO_6 and Sr_2InNbO_6 have been refined using neutron powder diffraction data. The resulting refined crystal structures agree well with those predicted previously using bond valence sum considerations. Kinetic factors are believed to be responsible for the inability to obtain the true 1:1 Ca_2InNbO_6 material under the synthesis conditions used. Instead, a wide-ranging 'solid solution' was found to span the composition range from $Ca_2[(Ca_{0.67}Nb_{0.33})Nb]O_6$ to just short of $Ca_2[InNb]O_6$. The crystal structures of two members of this 'solid solution' have also been successfully refined from powder neutron diffraction data.

The fact that $2Ca^{2+}$ and $1Nb^{5+}$ ions are able to substitute for $3In^{3+}$ ions on the B-sites of the Ca compounds is an intriguing phenomenon and attests to the well-documented structural flexibility of the perovskite

Table 4
Refined atomic positions (x,y,z), isotropic thermals (B_{iso}) and fractional site occupancies (Occ) of the atoms in $Ca_2[(Ca_{0.50}In_{0.25}Nb_{0.25})Nb]O_6$

Atom	x	y	z	B_{iso}	Occ
Ca	0.5118(5)	−0.0523(4)	0.2512(8)	1.36(4)	1.00
	0.5000	0.0000	0.2500		1.00
In	0.0000	0.0000	0.0000	0.56(3)	0.25
	0.0000	0.0000	0.0000		1.00
Nb	0.0000	0.0000	0.5000	0.58(3)	0.50
	0.0000	0.0000	0.5000		0.50
O1	0.3150(4)	0.7896(4)	0.9469(5)	1.30(2)	1.00
	0.3133	0.7907	0.9480		1.00
O2	0.2104(4)	0.3150(4)	0.9469(9)	1.30(2)	1.00
	0.2093	0.3133	0.9480		1.00
O3	0.1062(4)	0.0427(3)	0.2597(6)	1.30(2)	1.00
	0.1040	0.0000	0.2613		1.00
Nb2	0.0000	0.0000	0.0000	0.58(3)	0.25
	—	—	—	—	—
Ca2	0.0000	0.0000	0.0000	0.58(3)	0.50
	—	—	—	—	—

Space group $P12_1/n1$, $a = 5.5477(2)$ Å, $b = 5.7470(2)$ Å, $c = 7.9714(3)$ Å, $\beta = 89.958(3)^\circ$. The second row shows the starting values for the refinement taken from [6].
Refinement statistics: $\chi^2 = 2.26$, $R_{Bragg} = 2.01$, $R_p = 3.82$, $R_{wp} = 4.78$.

structure type. In terms of the optimisation of physical properties, the existence of *B*-site variable 'solid solution' fields such as the one reported here, leave open the possibility of continuously changing composition in order to tune physical properties.

Acknowledgments

The Authors would like to thank Dr. Margaret Elcombe and Dr. Andrew Studer (of the Australian Nuclear Science and Technology Organisation) for their help with collection of the neutron data, Dr. Darren Goossens for his expertise with Rietica, Dr. Frank Brink (of the Australian National University Electron Microscope Unit) for his help with EPMA analyses and also the Australian Institute of Nuclear Science and Engineering for their financial support (AINSE Award 2005, project no. 05176). YL and RLW acknowledge the Australian Research Council (ARC) for financial support in the form of an ARC Discovery Grant.

References

[1] J. Yin, Z. Zou, J. Ye, J. Phys. Chem. B 107 (2003) 61–65.
[2] I.M. Reaney, E.L. Colla, N. Setter, Jpn. J. Appl. Phys. 33 (1994) 3984–3990.
[3] L. Abdul Khalam, H. Sreemoolanathan, R. Ratheesh, P. Mohanan, M.T. Sebastian, Mater. Sci. Eng. B 107 (2004) 264–270.
[4] F. Galasso, W. Darby, J. Phys. Chem. 66 (1962) 131–132.
[5] V.F. Sears, Neutron News 3 (1992) 26–37.
[6] V. Ting, Y. Liu, R.L. Withers, E.R. Krausz, J. Solid State Chem. 177 (2004) 979–986.
[7] M.T. Anderson, K.B. Greenwood, G.A. Tayloer, K.R. Poeppelmeier, Prog. Solid State Chem. 22 (1993) 197–233.
[8] C.J. Howard, B.J. Kennedy, P.M. Woodward, Acta Crystallogr. B 59 (2003) 463–471.
[9] I. Levin, J.Y. Chan, J.E. Maslar, T.A. Vanderah, S.M. Bell, J. Appl. Phys. 90 (2001) 904–914.
[10] L.A. Bendersky, I. Levin, R.S. Roth, A.J. Shapiro, J. Solid State Chem. 160 (2001) 257–271.
[11] P.K. Davies, Curr. Opin. Solid State Mater. Sci. 4 (1999) 467–471.
[12] B. Noläng, Inst. Materialkemi, Ångströmlaboratoriet, Uppsala, Sweden.
[13] B.A. Hunter, Reitica—A Visual Reitveld Program, Commission on Powder diffraction Newslettter, vol. 20, 1969, p. 21.
[14] R.D. Shannon, C.T. Prewitt, Acta Crystallogr. B 25 (1969) 925.
[15] A.M. Glazer, Acta Crystallogr. B 28 (1972) 3384–3392.
[16] I. Levin, L.A. Bendersky, J.P. Cline, R.S. Roth, T.A. Vanderah, J. Solid State Chem. 150 (2000) 43–61.
[17] I. Levin, J.Y. Chan, R.G. Geyer, J.E. Maslar, T.A. Vanderah, J. Solid State Chem. 156 (2004) 122–134.
[18] V. Ting, Y. Liu, L. Norén, R.L. Withers, D.J. Goossens, M. James, C. Ferraris, J. Solid State Chem. 177 (2004) 4428–4442.